Acta Materialia 317 (2026) 122494

Contents lists available at ScienceDirect

Acta Materialia

journal homepage: www.elsevier.com/locate/actamat

Full length article

Shear-coupled grain growth statistics

Caihao Qiu [a,b], David J. Srolovitz [a,c], Gregory S. Rohrer [d,1], Jian Han [b,*], Marco Salvalaglio [e,f,*]

[a] Department of Mechanical Engineering, The University of Hong Kong, Pokfulam, Hong Kong Special Administrative Region of China
[b] Department of Materials Science and Engineering, City University of Hong Kong, Hong Kong Special Administrative Region of China
[c] Materials Innovation Institute for Life Sciences and Energy (MILES), The University of Hong Kong, Shenzhen, China
[d] Department of Materials Science and Engineering, Carnegie Mellon University, Pittsburgh, PA, USA
[e] Institute of Scientific Computing, TU Dresden, 01062 Dresden, Germany
[f] Dresden Center for Computational Materials Science, TU Dresden, 01062 Dresden, Germany

ARTICLE INFO

Keywords:
Grain growth
Shear coupling
Grain boundaries
Microstructure evolution
Phase field modeling
Internal stress

ABSTRACT

Grain growth (GG), mediated by grain boundary (GB) migration, is a fundamental mechanism of microstructure evolution in polycrystalline materials. GB migration is frequently accompanied by a relative shear displacement of grains meeting at GBs, a phenomenon known as shear-coupling. This coupling induces internal stresses within the microstructure, which recent studies have shown to play a decisive role in dictating microstructure evolution and GG pathways. This work provides a detailed characterization of the statistical features of two-dimensional GG in the presence of GB shear-coupling through continuum modeling of GB migration that incorporates fundamental microscopic mechanisms and diffuse-interface simulations. We demonstrate that incorporating shear-coupling produces a more heterogeneous, less equiaxed microstructure than conventional curvature-driven GG, while yielding topological and geometric properties consistent with experimental and atomistic observations. We further demonstrate that as grain grows in this regime, internal stress relaxes. Highly stressed grains shrink faster, and lightly stressed grains grow faster than other grains. These findings demonstrate that internal stress, an intrinsic feature of GG, profoundly changes essential features of GG microstructure and kinetics, consistent with experiments and atomic-scale simulations. Moreover, we discuss their implications for GG regimes and scaling behavior.

1. Introduction

Polycrystals are the most common type of engineering material, composed of crystalline domains (grains) with different crystallographic orientations separated by grain boundaries (GBs). The size, morphology, and topology of grains critically influence macroscopic material properties. Among the various mechanisms of microstructure evolution in polycrystals, grain growth (GG) plays a particularly prominent role. It occurs during thermal and thermomechanical treatments over a wide range of temperatures and length scales and is often deliberately exploited to engineer the grain size distribution and crystallographic texture, or suppressed to stabilize fine-grained microstructures.

The primary driving force for GG is capillarity. Since GBs are crystal defects with a positive excess energy, they migrate, particularly at elevated temperatures, to reduce the total GB area. This driving force leads to GB migration towards their centers of mean curvature; this is mean curvature or capillarity-driven flow. Microstructure evolution during isotropic GG has been well characterized over the past several decades (e.g., see [1]). Anisotropic GB energies and mobilities produce weighting factors on the curvature, amongst other effects such as faceting. The collective outcome of this GB migration is a progressive decrease in the number of grains and a corresponding increase in the average grain volume, as established by classical theories of normal GG [2–5] (the effect of GB anisotropy on GG has also been examined [6,7]). A number of experiments, atomistic simulations, and analyses, however, point to additional effects which cannot be simply ascribed to anisotropic GB energy or mobilities, including stress-driven GG [8–10] and grain rotation during GG [11–14], and effective mobilities poorly correlating with GB degrees of freedom [15,16].

Grain boundary migration is often accompanied by shear translations of one grain relative to another across GBs, a phenomenon known as shear-coupled migration [17]. This phenomenon is mechanistically

* Corresponding authors.
E-mail addresses: jianhan@cityu.edu.hk (J. Han), marco.salvalaglio@tu-dresden.de (M. Salvalaglio).

[1] Gregory S. Rohrer was an Editor of the journal during the review period of the article. To avoid a conflict of interest, Gregory S. Rohrer was blinded to the record and another editor processed this manuscript.

https://doi.org/10.1016/j.actamat.2026.122494
Received 13 March 2026; Received in revised form 13 June 2026; Accepted 23 June 2026
Available online 9 July 2026

described by the flow of line defects that glide along GBs and have step and/or dislocation character, namely disconnections [18–20]. The step nature of disconnections describes GB curvature, and their motion leads to curvature flow. Moreover, disconnection motion generates internal stress and couples to external stress owing to their Burgers vectors [21]. Disconnections have been widely observed on GBs [22,23] and heterophase interfaces [24–26]. The generation of internal stresses within the microstructure during GG has been observed in experiments [14,27] and atomistic simulations [28,29].

Phenomenological models have been developed to incorporate the effects of mechanical stress into GB migration and to assess its impact on GG. In one class of approaches, GBs are modeled in terms of geometrically necessary dislocations (GNDs), which can describe grain rotation and stress-driven GG [30,31]. Other formulations explicitly account for dislocation densities stored within grains, such that differences in the associated elastic energy across a GB act as an additional thermodynamic driving force for GB migration [32]. Elastic energy contributions associated with shear-coupled GB migration have also been introduced by effectively assigning a shear-coupling factor to individual grains, resulting in a shear-coupling "jump" at the boundary [33] and have been included in reduced-order modeling of microstructure evolution [34]. We recently extended a bicrystallography-respecting description of disconnection-mediated GB migration to microstructure evolution [35,36]. This framework uniquely enables the study of relatively large microstructures consistent with observed microscopic mechanisms of GB migration. This work demonstrated that GB shear-coupling and the resulting internally generated stresses are essential ingredients for a realistic description of GG, in quantitative agreement with both experimental observations and atomistic simulations [37].

Despite this significant progress, a comprehensive understanding of how internal and external stresses shape GG and its microstructures, as well as how internal stresses evolve in space and time, remains lacking. Large-scale characterization of GG has been effectively described through statistical analyses of the geometric and topological properties of the microstructure [38]. Such characterizations have been extensively reported from experimental measurements [39–41]. On the theoretical and numerical side, capillarity-driven microstructure evolution has been investigated using Monte Carlo Potts model [42–44], phase-field methods [45–47], and front-tracking simulations [1,48–50]. Nevertheless, systematic discrepancies persist between microstructure statistics obtained from experiments or atomistic simulations and those predicted by classical curvature-driven models [41,46,51,52], pointing to missing physical ingredients that are required for a realistic description of GG.

In this work, we focus on the question "how do shear-coupling phenomena affect grain growth?" To this end, we perform two-dimensional simulations of microstructure evolution both with and without shear-coupling and compare the resulting GG behavior. Since microstructure evolution is influenced by the coupling of stress and GB migration, we examine the effects of both internal stress (generated by shear-coupling and varying spatially through the microstructure) and external/applied stress (uniform through the material) on GG. In real materials, GG may also be strongly influenced by other effects, such as solute drag. The stresses may additionally arise from plastic deformation within grains, phase transformations, anisotropic elasticity, ...We do not include these factors in our simulations since their impact would cloud the interpretation of the shear-coupling effects on GG, the central focus of this work. Although such effects may play important roles in microstructure evolution and could be incorporated through extensions of the present simulation framework and/or atomistic simulations, this is beyond the scope of the present work.

2. Methods

We exploit a multi-phase field (PF) model that reproduces GB migration following the equation of motion in the presence of disconnection flow [35,53], as proposed in our earlier studies [36,37]. In brief, the polycrystalline microstructure is characterized by a set of order parameter fields $\boldsymbol{\eta}(\mathbf{x}) = \{\eta_1(\mathbf{x}), \eta_2(\mathbf{x}), \dots, \eta_i(\mathbf{x}), \dots, \eta_{N_g}(\mathbf{x})\}$, where $\mathbf{x} \in \Omega \subset \mathbb{R}^2$ and N_g is the total number of grains. The order parameter η_i represents the local volume fraction of grain i; hence, a local constraint must be imposed [54,55]: $\sum_{i=1}^{N_g} \eta_i(\mathbf{x}) = 1$. Inside grain i, $\eta_i = 1$ and $\eta_j = 0$ for $j \neq i$. At the GB between grains i and j, $\eta_i\eta_j > 0$, and $\eta_k = 0$ for $k \neq i, j$. At the triple junction (TJ) among grains i, j, and k, $\eta_i\eta_j\eta_k > 0$, $\eta_h = 0$ for $h \neq i, j, k$.

Following the multi-phase-field formulation established by Steinbach and co-workers for capillarity-driven evolution [54,55], and subsequently extended to incorporate shear-coupling [36,37], the evolution of the order parameter field η_i is given by

$$\frac{\partial \eta_i}{\partial t} = \sum_{j=1}^{N_g} M_{ij} \left(f_{\mathrm{GB}} + f_{\mathrm{bulk}} + f_{\mathrm{elastic}} \right), \tag{1}$$

$$f_{\mathrm{GB}} = \gamma_{ij} \left[\eta_j \nabla^2 \eta_i - \eta_i \nabla^2 \eta_j - \frac{\pi^2}{2\epsilon^2} \left(\eta_j - \eta_i \right) \right], \tag{2}$$

$$f_{\mathrm{bulk}} = \frac{\pi}{\epsilon} \sqrt{\eta_i \eta_j} \left(\psi_j - \psi_i \right), \tag{3}$$

$$f_{\mathrm{elastic}} = \boldsymbol{\tau} \cdot \boldsymbol{\beta}_{(i,j)} \left| \nabla \eta_j \right| \left[\hat{\mathbf{n}}(\eta_i) \cdot \hat{\mathbf{n}}(\eta_j) \right], \tag{4}$$

where M_{ij} and γ_{ij} refer to, respectively, the mobility and GB energy density of the GB between grains i and j, ϵ is a parameter related to the GB thickness in the diffuse-interface description, and ψ_i and ψ_j are the bulk free energy densities of grains i and j. In the absence of the elastic driving force f_{elastic}, the GB dynamics reduces to mean-curvature flow, thus reproducing the overall evolution associated with decreasing GB energy, as discussed elsewhere [47,55]. The vector $\boldsymbol{\tau}$ encodes the shear stresses resolved to the reference GBs, with $\boldsymbol{\tau} \equiv (\tau^{(k)}, \tau^{(k+1)})$, where k and $k+1$ index the low-energy reference GBs (chosen from a prescribed set) whose inclinations are closest to that of the GB between grains i and j [35]. The vector $\boldsymbol{\beta}_{(i,j)} \equiv (\beta^{(k)}_{(i,j)}, \beta^{(k+1)}_{(i,j)})$ contains the shear-coupling factors corresponding to the reference GBs. The vector $\boldsymbol{\tau}$ is given by the superposition of internal stresses (int) and externally applied stresses (ext): $\boldsymbol{\tau} = \boldsymbol{\tau}^{\mathrm{int}} + \boldsymbol{\tau}^{\mathrm{ext}}$. Here, $\boldsymbol{\tau}^{\mathrm{ext}}$ is a constant and $\boldsymbol{\tau}^{\mathrm{int}}$ is computed as the stress field generated by a distribution of disconnections, characterized by their shear-coupling factors, along the entire GB network, following the formulation developed in our previous studies [35–37].

The 2D polycrystalline microstructures in our simulations are assumed to be a cross-section through a $\langle 110 \rangle$ columnar microstructure of a face-centered cubic (FCC) material. For this polycrystal, GBs can be described in terms of an inclination between two symmetric tilt GBs (with normals [001] and $[1\bar{1}\bar{2}]$); i.e., a two-reference system description [35]. The local GB shear-coupling factor vector $\boldsymbol{\beta}_{(i,j)}$ is determined by the GB misorientation angle $\Delta\theta_{ij} = \theta_i - \theta_j$ (the inclination dependence is automatically accounted for in the two-reference system description) according to [21]:

$$\beta^{(1)}_{(i,j)}(\Delta\theta_{ij}) = \begin{cases} 2S\tan\left(\dfrac{\Delta\theta_{ij}}{2}\right), & 0 \le \Delta\theta_{ij} < \alpha_1 \\ 2S\tan\left(\dfrac{\Delta\theta_{ij} - \alpha_0}{2}\right), & \alpha_1 \le \Delta\theta_{ij} < \alpha_2 \\ 2S\tan\left(\dfrac{\Delta\theta_{ij} - \pi}{2}\right), & \alpha_2 \le \Delta\theta_{ij} < \pi \end{cases}, \tag{5}$$

$$\beta^{(2)}_{(i,j)}(\Delta\theta_{ij}) = \beta^{(1)}_{(i,j)}(\pi - \Delta\theta_{ij}), \tag{6}$$

where $\beta^{(1)}_{(i,j)}$ and $\beta^{(2)}_{(i,j)}$ are the shear-coupling factors of the two symmetric reference GBs, $\alpha_0 = 2\tan^{-1}(\sqrt{2})$ (i.e., the misorientation angle of an incoherent twin GB in FCC), $\alpha_1 = 7\pi/18$, $\alpha_2 = 5\pi/6$, and S is a scaling factor (see below).

The parameters used in this work are summarized in Table 1. We consider four simulation cases: (i) GG driven by curvature flow without internal stress (γ), (ii) GG driven by curvature flow and internal stress ($\gamma, \sigma^{\mathrm{int}}$), (iii) GG driven by curvature flow, internal stress, and applied shear stress ($\gamma, \sigma^{\mathrm{int}}, \sigma^{\mathrm{ext}}_{12}$), and (iv) GG driven by curvature flow, internal

Table 1
Dimensionless parameters used in the simulations. In the first column, γ, $\sigma^{\rm int}$, and $\sigma_{ij}^{\rm ext}$ are labels identifying different simulation settings: γ indicates the case with isotropic GB energy, $\sigma^{\rm int}$ indicates the case in which internal stress is included, and $\sigma_{ij}^{\rm ext}$ indicates the case in which an external stress with a nonzero ij component is applied.

Case	GB energy, γ	GB mobility, M	Shear modulus	Nonzero component of applied stress
γ	1	$\pi^2/(2\epsilon) \approx 0.1$	0	–
$\gamma, \sigma^{\rm int}$	1	$\pi^2/(2\epsilon) \approx 0.1$	6	–
$\gamma, \sigma^{\rm int}, \sigma_{12}^{\rm ext}$	1	$\pi^2/(2\epsilon) \approx 0.1$	6	$\sigma_{12}^{\rm ext} = 0.3$
$\gamma, \sigma^{\rm int}, \sigma_{11}^{\rm ext}$	1	$\pi^2/(2\epsilon) \approx 0.1$	6	$\sigma_{11}^{\rm ext} = 0.3$

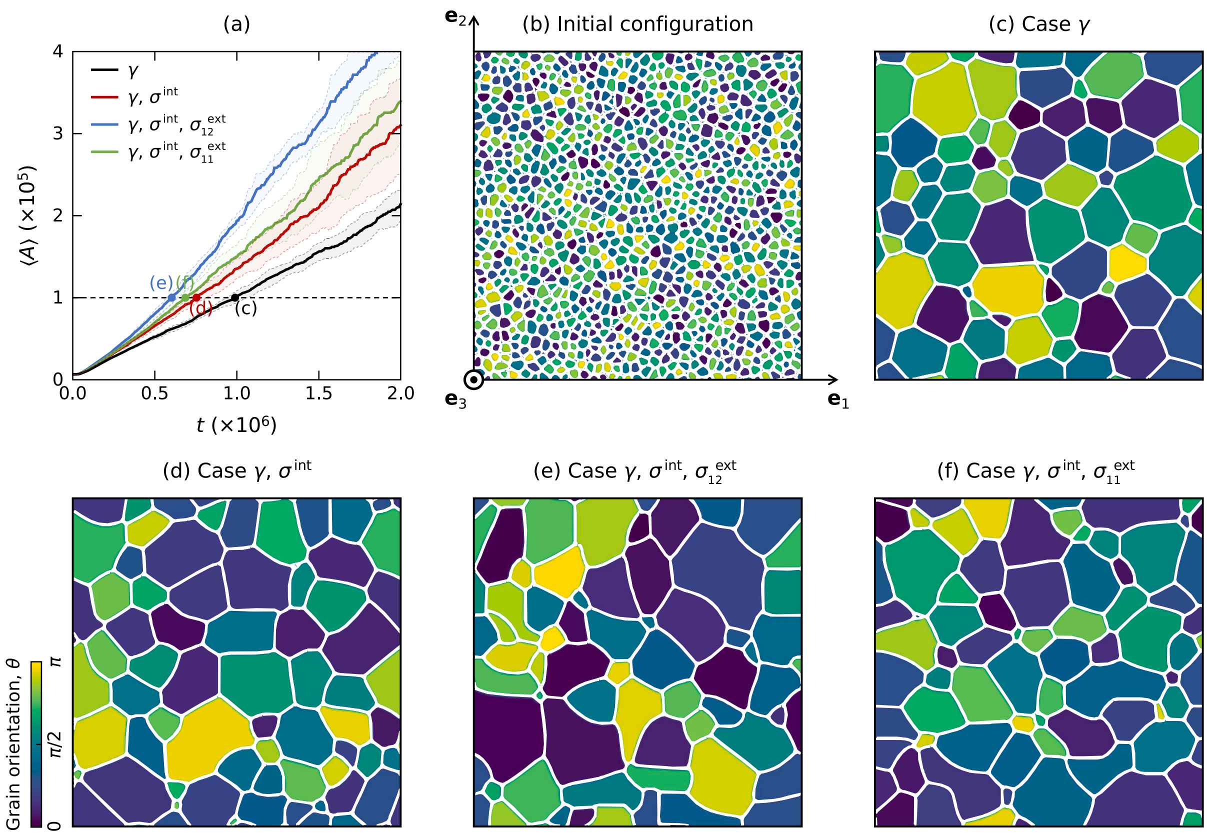

Fig. 1. (a) Mean grain size (area) $\langle A\rangle$ vs. time t during grain growth. Each curve is averaged over 10 independent PF simulations with and without internal stress ($\sigma^{\rm int}$) and applied external stress ($\sigma^{\rm ext}$). The shaded regions indicate the standard deviation. (b) Initial microstructure (with a white GB network and colored orientation θ field) of a typical 1000-grain polycrystal. All microstructures are shown at the same mean grain area $\langle A\rangle \approx 1\times10^5$ (indicated by the horizontal dashed line in (a)), which evolved from the initial microstructure in the cases (c) of mean curvature flow (γ), (d) with $\sigma^{\rm int}$ and no $\sigma^{\rm ext}$, (e) with $\sigma^{\rm int}$ and applied shear stress $\sigma_{12}^{\rm ext}$, and (f) with $\sigma^{\rm int}$ and applied tensile stress $\sigma_{11}^{\rm ext}$. (For interpretation of the references to color in this figure legend, the reader is referred to the web version of this article.)

stress, and applied tensile stress ($\gamma, \sigma^{\rm int}, \sigma_{11}^{\rm ext}$). The dimensionless parameters employed in the simulations are chosen to be approximately representative of aluminum. However, in this study we explicitly assume isotropic GB energies in order to isolate how shear-coupled GB migration modifies conventional mean-curvature flow (i.e., the von Neumann–Mullins relation). We set $S = 0.033$ to account for the observation that shear-coupling factors in polycrystals are smaller than those in bicrystals (by roughly this amount, associated with activation of multiple disconnection modes induced by the TJ constraints); see [22,27,28].

We employ the following non-dimensionalization of variables in the simulations: (length) $\tilde{\mathbf{x}} = \mathbf{x}/a_0$, (time) $\tilde{t} = tM_0\gamma_0/a_0^2$, (GB mobility) $\tilde{M} = M/M_0$, (stress) $\tilde{\sigma} = \sigma a_0/\gamma_0$, (bulk energy density) $\tilde{\psi} = \psi a_0/\gamma_0$, and (GB energy) $\tilde{\gamma} = \gamma/\gamma_0$, where $a_0 = 1$ nm and $\gamma_0 = 1$ J/m^2. The simulation cell is chosen to be square and is discretized into 250 × 250 grid points with uniform discretization $\delta x_1 = \delta x_2 = \epsilon/5 = 10$. Numerical simulations are performed by integrating Eq. (1) with time steps $\Delta t = 10$ via a simple finite-difference scheme.

The initial microstructures for PF simulations are Voronoi tessellations generated from 1000 randomly distributed (Poisson-distributed) points; an example is shown in Fig. 1(b). For each case of simulation settings, we generate 10 independent initial microstructures with randomly distributed GB networks and grain orientations; e.g., see Fig. 1(b). The results reported below are averages over the evolution of these 10 independently generated initial configurations.

3. Results

3.1. Grain size evolution

We first illustrate the impact of internal stress and applied external stress on GG; namely, the scaling of grain size with time in four different simulation cases as mentioned above. Fig. 1 shows the evolution of the mean grain area $\langle A\rangle$ during GG, along with the evolving microstructures, for the four cases.

Fig. 1(a) shows that including internal stresses accelerates GG, and applying external (both shear and tensile) stresses accelerates it further.

Table 2
Fitting parameters of the mean grain area vs. time data in the form $\langle A\rangle = K_A t^{n_A}$.

Case	K_A	n_A
γ	9.460 ± 0.247	1.006 ± 0.003
$\gamma, \sigma^{\mathrm{int}}$	4.429 ± 0.073	1.125 ± 0.002
$\gamma, \sigma^{\mathrm{int}}, \sigma_{12}^{\mathrm{ext}}$	3.022 ± 0.094	1.201 ± 0.003
$\gamma, \sigma^{\mathrm{int}}, \sigma_{11}^{\mathrm{ext}}$	3.565 ± 0.092	1.157 ± 0.003

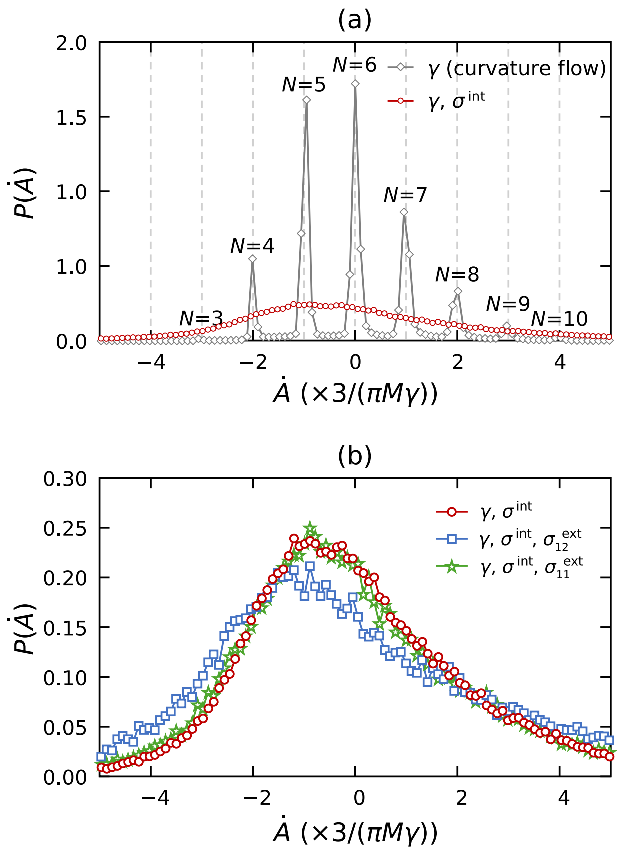

Fig. 2. Probability distribution of growth rates of individual grains in the cases (a) of curvature flow γ (gray diamonds) and with internal stress $\gamma, \sigma^{\mathrm{int}}$ (red circles), and with additional applied external (b) shear stress $\gamma, \sigma^{\mathrm{int}}, \sigma_{12}^{\mathrm{ext}}$ (blue squares) and tensile stress $\gamma, \sigma^{\mathrm{int}}, \sigma_{11}^{\mathrm{ext}}$ (green stars). (For interpretation of the references to color in this figure legend, the reader is referred to the web version of this article.)

This is consistent with the experimental observation of stress-driven GG [8,9].

The evolution of mean grain size is commonly fitted to a power law $\langle A\rangle = K_A t^{n_A}$, where K_A is a constant and n_A is known as the GG exponent; the best fit parameters for our data are shown in Table 2. Normal GG (i.e., mean curvature flow) in an isotropic system leads to a GG exponent $n_A = 1$, in agreement with conventional GG theory [2]. However, when internal stresses, generated during GG, are included in the simulations, the GG exponent increases to $n_A \approx 1.125$; i.e., the rate of GG increases with time (we return to this observation in the Discussion). Application of an external (shear or tensile) stress further increases the GG exponent; this effect is more pronounced for applied shear than tension. Interestingly, while application of an external stress increases the GG exponent n_A, it lowers the GG prefactor K_A by an even greater factor. This is consistent with the well-known compensation effect in GG [56].

In the 1950s, von Neumann and Mullins [3,4] showed that mean curvature flow leads to the rate of growth of any grain (of area A) in a polycrystal described by

$$\dot{A} \equiv \frac{\mathrm{d}A}{\mathrm{d}t} = -2\pi M\gamma\left(1 - \frac{1}{6}N\right), \tag{7}$$

where N is the number of neighbors/sides of grains (this has been extended to all dimensions [5]). Hence, the distribution of GG rates during isotropic mean curvature flow $P(\dot{A})$ is discrete. This is consistent with our curvature flow PF simulations (see Fig. 2(a)) with minor broadening associated with the diffuse-interface nature of this simulation method. However, when internal stresses are included in the simulation, the GG rate distribution is completely different, as seen in Fig. 2(a). That is, with internal stresses, the growth rate distribution is completely smooth, with no remnants of the delta-function-like distribution associated with mean curvature flow and the classic von Neumann–Mullins relation. The smooth form of the GG rate distribution survives the application of external stresses, as seen in Fig. 1(b). Interestingly, the application of a shear stress shifts the GG rate distribution towards smaller growth rates, while the application of a tensile stress leaves it unchanged relative to curvature flow alone (Fig. 1(b)).

3.2. Microstructural topology and geometry

Figs. 1(c)–(f) show microstructures with a mean grain size of $\langle A\rangle \approx 1 \times 10^5$ that evolved from the same initial configuration in Fig. 1(b) for the four simulation cases. As expected from the assumptions of elastic isotropy and isotropic GB energies and mobilities, the texture remained random throughout the simulations. Still, while all of the microstructures appear very similar (i.e., GBs meet at 120°, 6 sides per grain on average, …), there are also notable differences; e.g., the GBs appear more curved, and grains are less equiaxed when stress effects are included. In this section, we characterize the effects of internal and external stresses on the geometrical and topological features of evolved microstructures.

The topological characteristics of a 2D microstructure are commonly described by the probability distribution of the number of grain neighbors (or sides), $P(N)$. In PF simulations, $P(N)$ peaks at $N = 6$ when GG is driven solely by mean-curvature flow (see the solid line in Fig. 3(a)), consistent with previous independent numerical studies, such as the front-tracking (sharp-interface) results shown by the thick dashed line in Fig. 3(a) [1]. (Note, the front-tracking simulations are based on a thousand times as many grains as our PF simulations, so they should be viewed as more accurate than our PF results; nonetheless, the agreement is excellent.) When GB shear-coupling and internal stress are included, the peak of $P(N)$ shifts from $N = 6$ to $N = 5$ (see Fig. 3(b)). Comparison of the PF GG simulations results with experiment [40,41] and diffusive-timescale "atomistic" (phase field crystal, PFC) simulations [52] shows very good agreement only when internal stresses are included. In particular, note that the peaks in the side distributions obtained from the experiments, atomistic simulations, and PF simulations with internal stress included are all at $N = 5$ (Fig. 3), rather than $N = 6$ (see Fig. 3(a) for two sets of mean-curvature flow simulations).

Another common descriptor of the microstructure is the grain size distribution (probability distribution of the reduced grain size), $P(\mathcal{R}/\langle\mathcal{R}\rangle)$, where $\mathcal{R} = \sqrt{A}$. For isotropic curvature-driven GG, $P(\mathcal{R}/\langle\mathcal{R}\rangle)$ exhibits two peaks, at $\mathcal{R}/\langle\mathcal{R}\rangle \approx 0.9$ and 1.2 (observed both in our PF simulations and in front-tracking simulations [1]); see Fig. 4(a). When GB shear-coupling and the resulting internal stress are included, these two peaks merge and shift towards a smaller grain size, $\mathcal{R}/\langle\mathcal{R}\rangle \approx 0.8$, as shown by the red curve in Fig. 4(b). Experiments and PFC simulations also display single-peak distributions, with peak locations in the range 0.7–0.8, cf. the red curve and the discrete symbols (circles [51], squares [41], and crosses [52]) in Fig. 4(b). When an external stress is applied, the grain size distribution retains the single peak; see Fig. 4(c). An applied shear has a much larger effect on the grain size distribution than the same magnitude tensile stress (Fig. 4), shifting the grain size distribution towards smaller grain size.

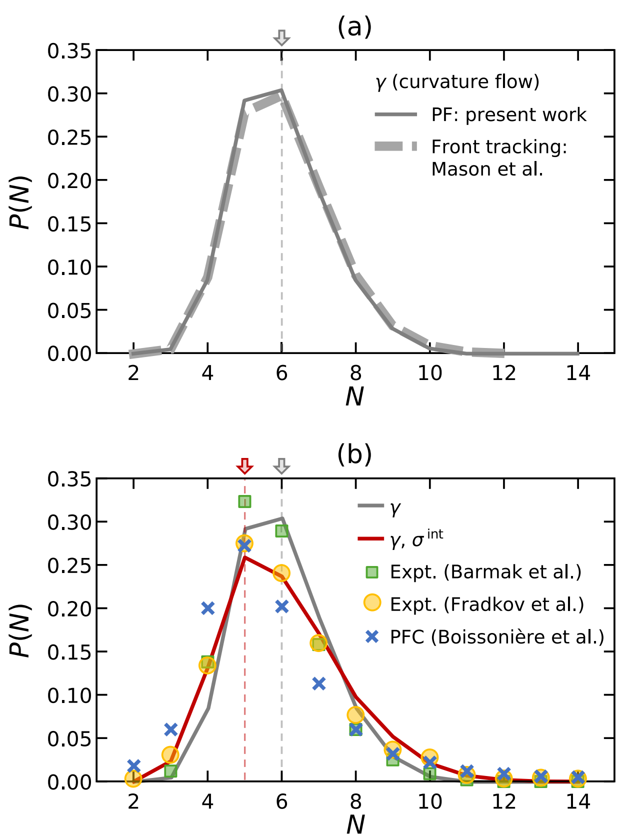

Fig. 3. Probability distributions of number of neighbors (N) of individual grains during GG described by (a) γ (curvature flow), where the solid and dashed lines represent the results from the present and previous front-tracking modeling work [1], respectively; and (b) Case $\gamma, \sigma^{\text{int}}$, where the orange circles, green squares, blue crosses, and the red line are the results from GG experiments in an Al thin film [40,41], PFC simulation [52], and the present work, respectively. (For interpretation of the references to color in this figure legend, the reader is referred to the web version of this article.)

We also examine several other descriptors of the grain geometry; i.e., the probability distribution of the grain roundness $P(\bigcirc)$, with the roundness defined as $\bigcirc = 4\pi A/\mathcal{C}^2$ (Figs. 4(d)-(f)), the reduced grain perimeter $P(\mathcal{C}/\langle\mathcal{C}\rangle)$ (Figs. S4a-c in supplementary material, SM), and the reduced GB length distribution $P(\mathcal{L}/\langle\mathcal{L}\rangle)$ (Figs. S4d-f in SM). All linear measures of grain size ($\mathcal{R}$, $\mathcal{C}$, $\mathcal{L}$) show the same trends with respect to the comparison of the curvature flow results and the inclusion of internal (and external) stresses (cf. Figs. 4 and SM Fig. S4). The roundness is a measure of compactness of the grain shape (i.e., how close the grain is to a circle). As seen in Fig. 4(e), the grain roundness distribution for isotropic curvature flow has a relatively sharp single peak with a maximum near $\bigcirc = 0.88$; this distribution broadens and shifts to smaller roundness (peak at $\bigcirc = 0.84$ when internal (and external) stresses are included in the PF simulations. Overall, we find that GG microstructure becomes more inhomogeneous in the presence of shear-coupling.

To quantify the degree of inhomogeneity, we examine several geometric properties of the simulated microstructure vs. mean grain size (or, equivalently, time – Fig. 1(a)); see Fig. 5. To describe the degree of GB faceting in the microstructure, we first calculate the degree of faceting of each GB as $\Delta\Phi/\phi_{\text{c}}$ [57] with

$$\Delta\Phi = \phi_{\text{c}} - \int \min_k \left|\phi(s) - \phi^{(k)}(s)\right| \,\mathrm{d}s \bigg/ \int \mathrm{d}s, \tag{8}$$

where the integral over s is along an entire GB, $\phi(s) = \arccos(\hat{\mathbf{l}}(s)\cdot\mathbf{e}_1)$ is the local inclination angle ($\hat{\mathbf{l}}(s)$ is the local tangent vector), and $\phi^{(k)} = 0$ for $k = 0$ and $\phi^{(k)} = \pi/2$ for $k = 1$. ϕ_{c} is the critical inclination angle when the GB is perfectly faceted, i.e., GBs are fully faceted when $\Delta\Phi/\phi_{\text{c}} = 1$, whereas $\Delta\Phi/\phi_{\text{c}} = 0$ corresponds to the absence of faceting. It is important to note that GB facets correspond roughly to the reference interfaces for shear-coupling. Note that for GBs with any anisotropy, these reference interfaces are highly coherent, relatively low-energy GB planes (corresponding to cusps in the GB energy versus inclination). Even though the GB energies are isotropic, the GB shear-coupling factors are anisotropic (inclination-dependent). This type of shear-coupling-induced faceting need not be consistent with that from anisotropic GB energies (i.e., the Wulff construction) [57]. This is consistent with the observed lack of consistency between facet orientations and GB energy anisotropy in experiment [58].

As seen in Fig. 5(a), the average degree of faceting $\langle\Delta\Phi\rangle/\phi_{\text{c}}$ remains near constant under curvature flow conditions. When internal stress and/or applied external stresses are included, GBs rapidly begin to facet, and the degree of faceting tends to increase over time. Since external stress drives GB motion in a direction that does not necessarily favor faceting, the degree of faceting under external stress (blue squares and green stars) is slightly smaller than that obtained when only internal stress is considered (red circles).

We also investigate the average grain aspect ratio $\langle\text{AR}\rangle$ (the best fit of each grain shape to an ellipse is determined, and the aspect ratio is the ratio of the major and minor axes); the deviation of grain aspect ratio from perfect equaixed morphology ($\langle\text{AR}\rangle - 1$) is shown in Fig. 5(b). Similar to the degree of faceting, the aspect ratio appears to approach a steady state in the case of curvature flow. However, when internal stresses are included in the microstructure evolution, $\langle\text{AR}\rangle - 1$ increases, consistent with the larger number of elongated grains visible in Fig. 1(d); external stress further amplify this effect (cf. Figs. 1(d)-(f)). This demonstrates that GB shear-coupling induces the formation of elongated grain shapes, even in the isotropic GB limit. This observation offers significant implications for interpreting experimental observation where anisotropic grain morphologies cannot be predicted from the GB energy anisotropy alone [7,59]. A related geometric quantity is the average grain roundness $\langle\bigcirc\rangle$; grains with larger aspect ratios naturally exhibit lower roundness. We plot the degree by which the grain shape deviates from being perfectly circular $\langle\Delta\bigcirc\rangle = 1 - \langle\bigcirc\rangle$ in Fig. 5(c). Consequently, the ranking of the average deviation from a circle for the four cases is: $\langle\Delta\bigcirc\rangle_{\gamma,\sigma^{\text{int}},\sigma^{\text{ext}}_{12}} > \langle\Delta\bigcirc\rangle_{\gamma,\sigma^{\text{int}},\sigma^{\text{ext}}_{11}} > \langle\Delta\bigcirc\rangle_{\gamma,\sigma^{\text{int}}} \gg \langle\Delta\bigcirc\rangle_{\gamma}$.

Our analysis of the various topological and geometric properties of the evolving microstructure shows that internal and applied external stresses drive pronounced deviations from an equiaxed grain morphology, leading instead to more elongated grains and increased inhomogeneity in the distributions of grain size, grain perimeter, and GB length.

3.3. Internal stresses within microstructures during grain growth

Given that internal stresses strongly modify GG, it is natural to ask: how do internal stresses evolve? Fig. 6 shows the temporal evolution of the average internal von Mises stress, $\langle\sigma_{\text{vM}}\rangle$. Fig. 6(a) shows that $\langle\sigma_{\text{vM}}\rangle$ decrease continuously during GG. To quantify this behavior, we fit the internal stress dependence on the mean grain size through $\langle\sigma_{\text{vM}}\rangle = K_\sigma\langle A\rangle^{-n_\sigma}$; the best fit parameters are shown in Table 3 and the fit is very good. Examination of Fig. 6(a) and the fact that $n_\sigma > 0$ show that the stress in the microstructure decays as grains grow; as the density of GBs tends to zero, so does the stress (recall that GB motion is the source of the internal stress through GB shear-coupling). It is interesting to observe that, with shear-coupling, the average internal stress decays roughly as $\langle\sigma_{\text{vM}}\rangle \sim \langle\mathcal{R}\rangle^{1/4}$ (while suggestive, we do not have a good model for such a relation). The relaxation of internal stress is slower in the cases with applied external stress than in those without, following an order opposite to that of the corresponding grain-growth rates (cf. Figs. 1(a) and 6(a)). Fig. 6(b) shows the probability distribution of the reduced internal von Mises stress, $P(\sigma_{\text{vM}}/\langle\sigma_{\text{vM}}\rangle)$. For cases both with

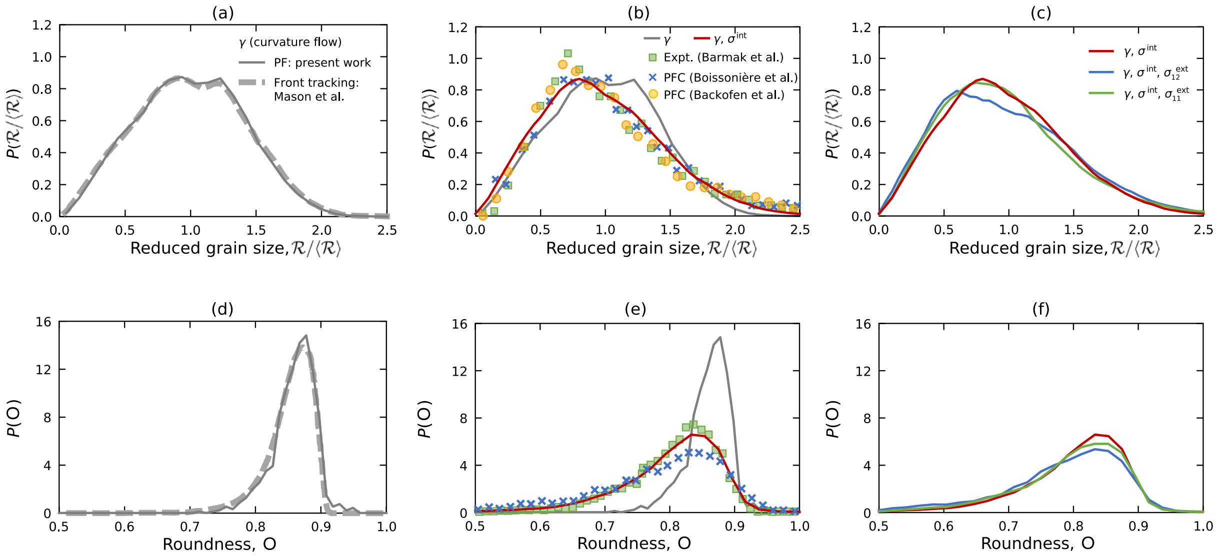

Fig. 4. Geometric properties of microstructures. probability distributions of (a)–(c) reduced grain size $\mathcal{R}/\langle\mathcal{R}\rangle$ and (d)–(f) grain roundness ○. The gray, red, green, and blue lines correspond to our PF results for the case of curvature flow with internal stress, external tensile stress, and external shear stress, respectively. The thick gray dotted lines in (a) and (d) are the results obtained by the front-tracking method [1]. Green squares, blue crosses, and yellow circles are the results from experiments in an Al thin film [41] and PFC simulations [51,52]. Note that each probability distribution is the averaged result based on microstructures with a mean grain area $\langle A\rangle > 5\times10^4$. (For interpretation of the references to color in this figure legend, the reader is referred to the web version of this article.)

Table 3
Fitted parameters of the internal stress vs. mean grain area data, $\langle\sigma_{\mathrm{vM}}\rangle = K_\sigma t^{n_\sigma}$.

Case	K_σ ($\times10^5$)	n_σ
$\gamma, \sigma^{\mathrm{int}}$	0.598 ± 0.002	0.129 ± 0.003
$\gamma, \sigma^{\mathrm{int}}, \sigma_{11}^{\mathrm{ext}}$	0.617 ± 0.004	0.107 ± 0.005
$\gamma, \sigma^{\mathrm{int}}, \sigma_{12}^{\mathrm{ext}}$	0.646 ± 0.004	0.094 ± 0.005

and without applied external stress, this distribution is log-normal-like and remains self-similar throughout GG (see Fig. S3).

As shown previously [37], the internal stress is spatially inhomogeneous, and there is a considerable stress accumulation at GBs and TJs. However, how internal stress evolves across different regions of the microstructure remains unclear. We show the evolution of internal stress within grains, at GBs, and at TJs (as defined by the magnitude of the order parameters in the PF model) in Fig. 7. The evolution of the average internal von Mises stress within grains and at GBs follows the same trend as that measured for the whole microstructure (Fig. 6(a)), i.e., stress relaxation during evolution, with slower decay under applied external stress. In contrast, the internal stress at TJs is noisy, but is roughly time- or $\langle A\rangle$-independent within the statistics of the simulation (Fig. 7(c)). In our continuum model, the origin of internal stress relaxation is the evolution of the disconnection Burgers vector density on GBs [35,36,60], and the stress in the grain interior is the long-range stress originating from shear-coupling. Therefore, it is not surprising that the internal stress evolution within grains and at GBs follows similar trends, with a relatively smaller stress magnitude and relaxation rate in grain interiors than GBs (due to the $\sim 1/r$ decay of the stress field away from disconnection cores on GBs [61]). However, TJs (with lower mobility than GBs) act as obstacles to GB migration, leading to disconnection pile-up at TJs and increased local internal stress [37,62]. The order of the stress relaxation rates obtained from our PF simulations, $\overline{\langle\sigma_{\mathrm{vM}}\rangle}_{\mathrm{GB}} > \overline{\langle\sigma_{\mathrm{vM}}\rangle}_{\mathrm{grain}} \gg \overline{\langle\sigma_{\mathrm{vM}}\rangle}_{\mathrm{TJ}}$, consistent with the argument above.

4. Discussion

The results reported above compare GG in the presence and absence of shear-coupling. We demonstrated that the associated internal stress generated by shear-coupling (i) significantly alters the evolving microstructure and (ii) itself evolves along with the microstructure evolution. In order to interpret these result, we now analyze how the evolution of microstructure co-evolves with internal stress, the impact of shear-coupling on GG kinetics, and the implications for more general GG regimes compared to the settings considered in the simulations presented here.

4.1. Co-evolution of internal stress and microstructure

The co-evolution of internal stress and the geometric descriptors of microstructure can be characterized by examining the variation of those descriptors with the averaged internal von Mises stresses, as shown in Fig. 8. All of these descriptors (the degree of faceting, grain aspect ratio, and deviation from a circle) decrease linearly with the averaged internal von Mises stress (see the fitted lines). While the grain shapes become more isotropic and faceting decreases with increasing average internal von Mises stress, application of an external stress (uniaxial or shear) changes the slopes as $|m|_{\gamma,\sigma^{\mathrm{int}}} < |m|_{\gamma,\sigma^{\mathrm{int}},\sigma_{11}^{\mathrm{ext}}} < |m|_{\gamma,\sigma^{\mathrm{int}},\sigma_{12}^{\mathrm{ext}}}$ (the opposite occurs for GB faceting). External stress strengthens this dependence for the deviation from a circle and aspect ratio, but weakens it for the degree of faceting. This is consistent with the effects of external stress on the evolution of the same properties with grain size as indicated in Fig. 5. These results demonstrate that the evolution of the geometric descriptors of the GG microstructure strongly depends on internal stress. We should note that the average von Mises stress in Fig. 8 increases from left to right, whereas time progresses from right to left (i.e., the mean grain size increases while the average von Mises stress decreases with time; see Fig. S5).

To gain further insight into the impact of stress on microstructure evolution, we examine the role of internal stress on the growth rate of individual grains. Fig. 9(a) shows the probability distributions of grain-growth rates, analogous to Fig. 2(b). We identify the 10% of the grains that grow the fastest and the 10% of the grains that shrink the fastest in Fig. 9(a). The fast-growing grains have $\dot{A} > 3.5$, indicated by blue while the fastest shrinking grains have $\dot{A} < -2.3$, indicated by green. The white histogram in Figs. 9(b) and (c) shows the probability distribution of the internal von Mises stress (with internal stress and no external stress applied), denoted by $P_{\sigma_{\mathrm{vM}}}$. In Figs. 9(b) and (c),

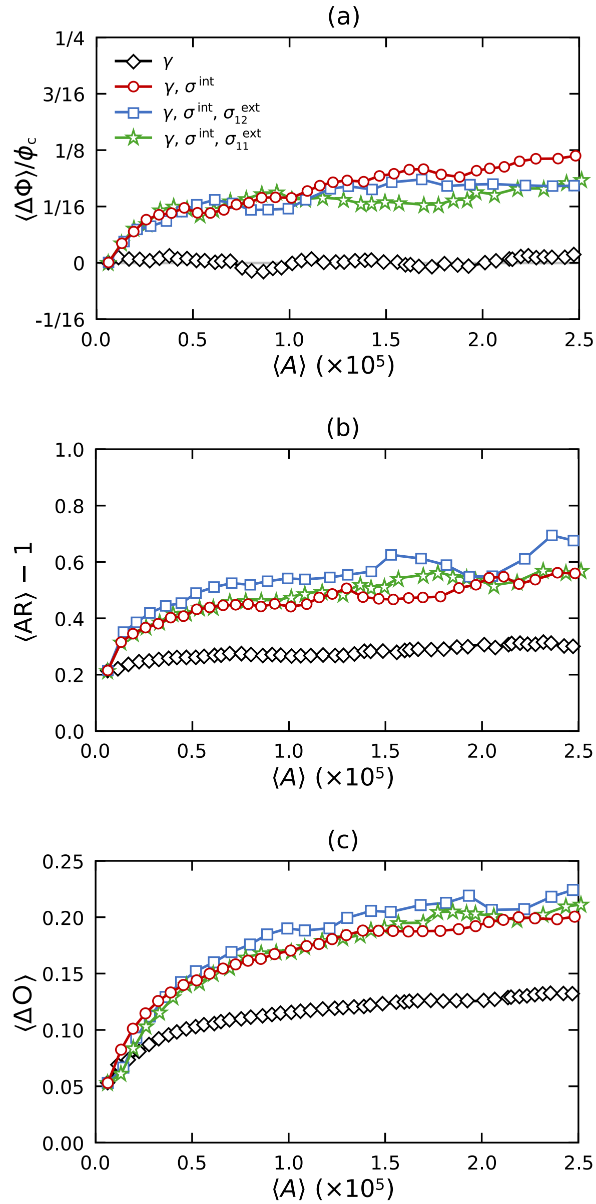

Fig. 5. Evolution of the average (a) GB degree of faceting $\langle \Delta\Phi \rangle/\phi_c$, (b) grain aspect ratio $\langle \mathrm{AR} \rangle - 1$ and (c) deviation from a circle $\langle \Delta \bigcirc \rangle$ vs. mean grain area in the cases of γ (curvature flow, black circles); $\gamma, \sigma^{\mathrm{int}}$ (red circles); $\gamma, \sigma^{\mathrm{int}}, \sigma^{\mathrm{ext}}_{11}$ (green stars); and $\gamma, \sigma^{\mathrm{int}}, \sigma^{\mathrm{ext}}_{12}$ (blue squares). (For interpretation of the references to color in this figure legend, the reader is referred to the web version of this article.)

the blue and green histograms show the von Mises stress distributions in, respectively, the fast-growing grains ($P^{+}_{\sigma_{\mathrm{vM}}}$) and the fast-shrinking grains ($P^{-}_{\sigma_{\mathrm{vM}}}$). According to the Bayes' theorem, the ratio $P^{+/-}_{\sigma_{\mathrm{vM}}}/P_{\sigma_{\mathrm{vM}}}$ measures the probability that a grain grows/shrinks fast when its von Mises stress is σ_{vM} (the factor 10% is omitted). The calculation results for $P^{+/-}_{\sigma_{\mathrm{vM}}}/P_{\sigma_{\mathrm{vM}}}$ are plotted as the hollow blue/green circles in Fig. 9b/c. The best linear fit to these data is represented by the solid lines. We find that fast-growing grains tend to be those with small internal stress (i.e., the negative correlation in Fig. 9(b)), whereas fast-shrinking grains tend to have large internal stress (i.e., the positive correlation in Fig. 9(c)).

To confirm that the inclusion of internal stress as a *driving force* in the microstructure evolution is the cause of the correlation between internal stress and GG rate as shown in Figs. 9(b) and (c), we performed

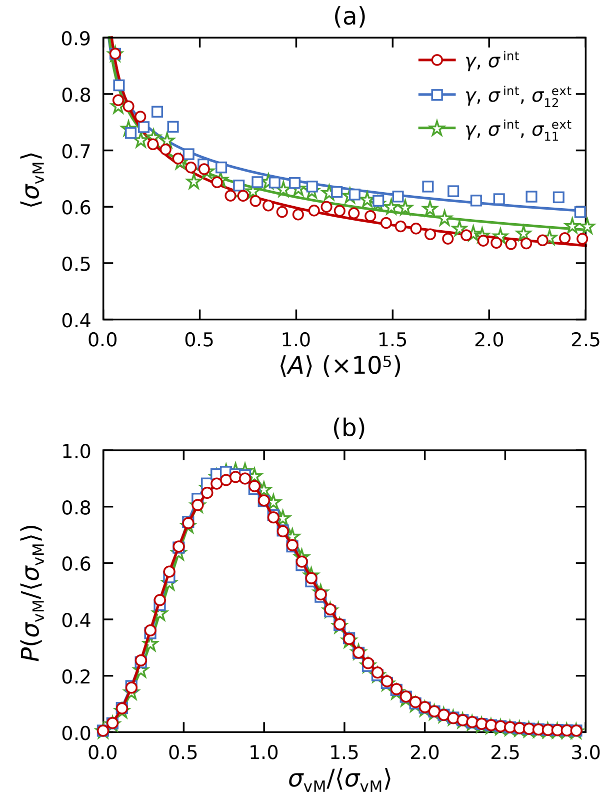

Fig. 6. The temporal evolution of the internal stress field in the cases of $\gamma, \sigma^{\mathrm{int}}$ (red circles), $\gamma, \sigma^{\mathrm{int}}, \sigma^{\mathrm{ext}}_{11}$ (green stars), and $\gamma, \sigma^{\mathrm{int}}, \sigma^{\mathrm{ext}}_{12}$ (blue squares). (a) Average internal von Mises stress ($\langle \sigma_{\mathrm{vM}} \rangle$) vs. mean grain area. (b) Probability distribution of reduced internal von Mises stress ($\sigma_{\mathrm{vM}}/\langle \sigma_{\mathrm{vM}} \rangle$). Note that each probability distribution is averaged over the microstructures with a mean grain area $\langle A \rangle > 5 \times 10^4$. (For interpretation of the references to color in this figure legend, the reader is referred to the web version of this article.)

a similar analysis for microstructure evolution only driven by capillarity (mean-curvature flow; see Figs. S6 in SM); the internal stress is computed but not included in the driving force for GB migration. These results show that internal stress and GG rate do not correlate unless internal stress is included as a driving force for GB migration.

4.2. Grain growth kinetics

In Section 3.1, Fig. 1(a) and Table 2, we found that the GG exponent is larger than 1 when internal stresses are considered (while in mean-curvature flow, the exponent is 1). To understand the origin of this phenomenon, we track the evolution of the average capillarity force (F_γ) and elastic driving force (F_σ) along all GB segments as a function of grain size during GG; see the red and blue circles in Fig. 10. We fit these data to the function $F \sim \langle \mathcal{R} \rangle^{n_F}$ (solid red and blue lines in the figure). According to conventional curvature-driven GG theory, the capillarity force scales inversely with the mean grain size (i.e., $F_\gamma \sim \langle \mathcal{R} \rangle^{-1}$). In contrast, $n_F = -0.51 \approx -1/2$ for the elastic driving force F_σ data. This difference in scaling implies that while capillarity dominates the early stages of growth when grains are small, elastic driving forces dominate GG kinetics at large grain sizes (this can also be seen by comparing the evolution of the probability distributions of the capillarity and elastic driving forces in Figs. S7a and b). The exponent $n_F \approx -0.5$ of the elastic driving force can be understood in terms of disconnection pile-ups at the triple junction, similar to the yield stress decaying as $\langle \mathcal{R} \rangle^{-0.5}$ when the bulk dislocations pile up at GBs in the Hall-Petch relation [63] (see the theoretical model developed in SM). The crossover point is around

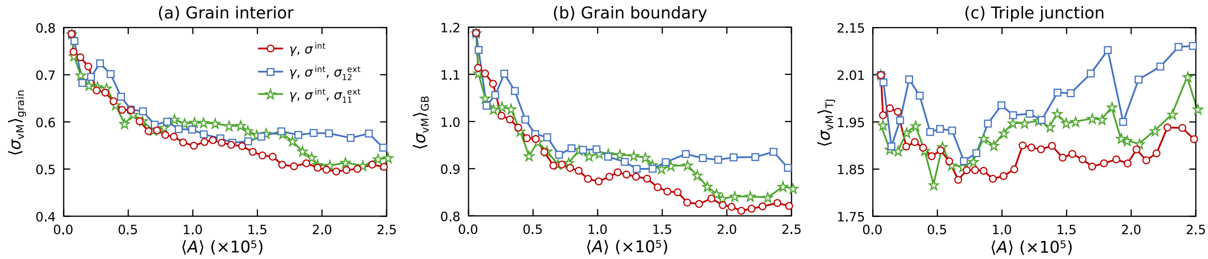

Fig. 7. The temporal evolution of the internal stress field (a) in grain interior, (b) at GBs, and (c) at TJs in the cases of $\gamma, \sigma^{\mathrm{int}}$ (red circles), $\gamma, \sigma^{\mathrm{int}}, \sigma_{11}^{\mathrm{ext}}$ (green stars), and $\gamma, \sigma^{\mathrm{int}}, \sigma_{12}^{\mathrm{ext}}$ (blue squares). (For interpretation of the references to color in this figure legend, the reader is referred to the web version of this article.)

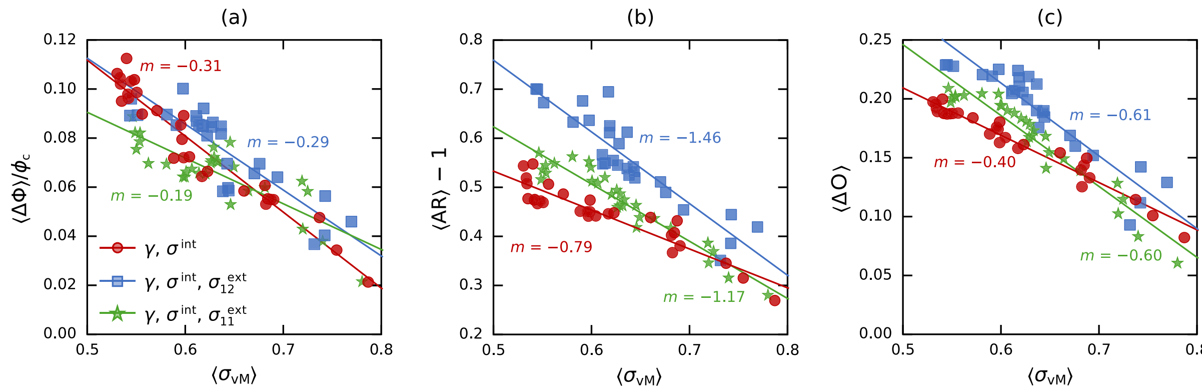

Fig. 8. (a) Degree of faceting $\langle \Delta\Phi \rangle/\phi_c$, (b) grain aspect ratio $\langle \mathrm{AR} \rangle - 1$, and (c) deviation from a circle $\langle \Delta\bigcirc \rangle$ versus the averaged internal von Mises stress. The cases are: $\gamma, \sigma^{\mathrm{int}}$ (red circles), $\gamma, \sigma^{\mathrm{int}}, \sigma_{11}^{\mathrm{ext}}$ (green stars), and $\gamma, \sigma^{\mathrm{int}}, \sigma_{12}^{\mathrm{ext}}$ (blue squares). Each data point is the microstructure average of a geometric property at a particular mean grain size. The solid lines are linear fits to the data, with the slope m determined. Note that, since GG is accompanied by a decay of $\langle \sigma_{\mathrm{vM}} \rangle$, time progresses from right to left along the $\langle \sigma_{\mathrm{vM}} \rangle$ axis. (For interpretation of the references to color in this figure legend, the reader is referred to the web version of this article.)

$\langle \mathcal{R} \rangle \approx 220$. If we fit the total force on GBs as a function of grain size $\langle \mathcal{R} \rangle$, we find $n_F = -0.64$, which is between these two limits.

If we assume $\mathrm{d}\langle \mathcal{R} \rangle/\mathrm{d}t \sim F$ [2], the GG law follows $\langle A \rangle = \langle \mathcal{R} \rangle^2 \propto t$ if the driving force is only F_γ and $\langle A \rangle = \langle \mathcal{R} \rangle^2 \propto t^{4/3}$ if only F_σ. Our numerical results for F_{tot} versus $\mathrm{d}\langle \mathcal{R} \rangle$ suggest that $n_A \approx 1.22$, which is $n_A \in [1, 4/3]$ when both capillarity force and elastic driving force are considered. Our fitted n_A results in Table 2 perfectly fall in this range and are consistent with the fitted force data in Fig. 10.

We note that since shear-coupled GB migration is influenced by the local stress, and that stress is concentrated at the triple junctions (TJs), GB migration near TJs is sensitive to boundary conditions at TJs. On the one hand, if TJs do not transmit disconnections from one GB at the TJ to the others (or not allow disconnection reactions there), disconnection pile-ups and local internal stress concentrations will be maximized. These pile-ups at the TJ may induce stresses that extend well beyond a few atomic spacings of the TJ itself. On the other hand, if disconnections on one GB are fully transmitted through the TJ to the adjoining GBs through barrier-less reactions, no (or only small) pile-ups or stress concentrations will form at the TJs, the mechanical constraint associated with TJs will be relaxed. Indeed, stress build-up as a result of mechanical constraints has been observed in atomistic simulations of GB migration in bicrystals [28]. This suggests that internal stress development during GG requires both shear-coupled migration and mechanical constraint such as that provided by TJs. For grain-growth in physical systems, where disconnections may react at TJs albeit with a barrier, the TJ mechanical constraint may be partially relaxed; i.e., the nature of the stress accumulation at the TJs will fall between the no-reaction and barrier-less reaction limits; with increasing temperature, relaxation through reactions will become more effective. While it is clear from the simulation data presented that incorporating shear-coupling accelerates grain growth kinetics beyond pure mean-curvature-driven growth, the effect may be somewhat more pronounced in the simulations than in physical materials. Perhaps the best way to investigate the effects of reactions at TJs currently is through large-scale, long-time molecular dynamics simulations. Nonetheless, the present simulations show the effect of a reaction barrier at TJs which is inevitable in all situations.

4.3. Implications for realistic grain growth

Although the characterization of grain growth microstructures (presented above) and their comparison with experiments, indicating that it is essential to include shear-coupling in the description of GG, it is surprising that the observed GG exponents are (slightly) greater than one rather than one or less in most experiments. A few remarks are in order. First, while both capillarity and shear-coupling driving forces (on average) decrease with increasing grain size, the capillarity driving force decreases faster with increasing grain size than that associated with shear-coupling. This suggests that grain growth may never be truly in steady-state and that the slightly greater than one exponents may simply represent a transition from the dominance of one type of driving force to the other; i.e., the kinetics is not robustly power-law at all. Second, given the small values of the deviation of our simulation exponents from unity, it may be that the extraction of exponents from classical experimental data may not be sufficiently accurate to reliably see such slightly larger exponents. We also note that since we do not know where the switch from the dominance of one type of driving force over the other occurs in a physical material, it is possible that most of the existing data is in one regime or the other. Finally, as discussed above, there are many physical effects in real materials that influence grain growth not included in these simulations (designed to isolate shear-coupling effects). These "other" effects may play increasingly important roles at larger grain size and hence slow down late time kinetics exactly where the shear-coupling effects tend to dominate.

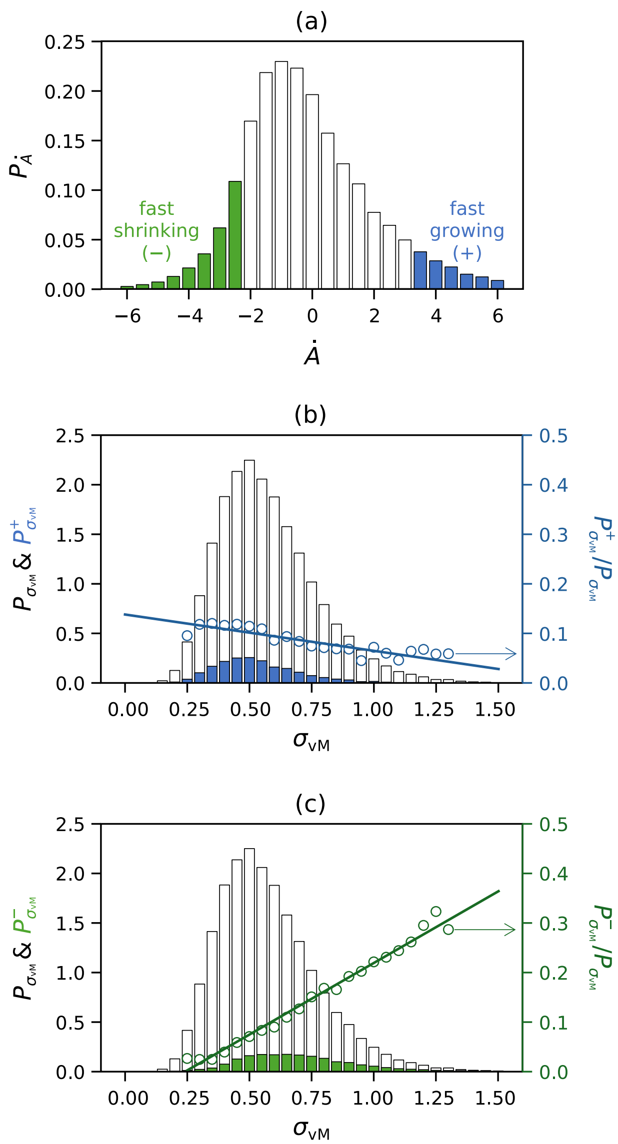

Fig. 9. (a) Probability distribution of the GG rates in the case of $\gamma, \sigma^{\text{int}}$. The regions shaded in blue and green correspond to the 10% of the grains that grow and shrink the fastest, respectively. (b, c) The white bars show the probability distributions of internal von Mises stress. The blue bars in (b) and green bars in (c) show the stress distributions in, respectively, the fast-growing and the fast-shrinking grains. The ratios, $P^+_{\sigma_{vM}}/P_{\sigma_{vM}}$ and $P^-_{\sigma_{vM}}/P_{\sigma_{vM}}$, are plotted as blue and green circles. The blue and green solid lines show the linear fits to the blue and green circles. (For interpretation of the references to color in this figure legend, the reader is referred to the web version of this article.)

In our continuum, shear-coupling (disconnection-based) approach, elastic anisotropy is neglected to reduce computational cost and complexity. Elastic anisotropy will have two effects on GB migration. First, the stress fields of dislocations in anisotropic elastic media will differ from those in isotropic media we used in this work [64]; this will modify the generated internal stress field and consequently the driving force for GB migration through the Peach–Koehler force. Second, elastic anisotropy can produce new driving forces on GB migration (i.e., difference in elastic energies and elastic mismatch among individual grains). Although the elastic energy difference across the GBs can serve as a driving force for GB migration [65], it is in higher order compared with the Peach–Koehler force (i.e., its magnitude should usually be negligible compared with the capillarity force and the elastic driving force

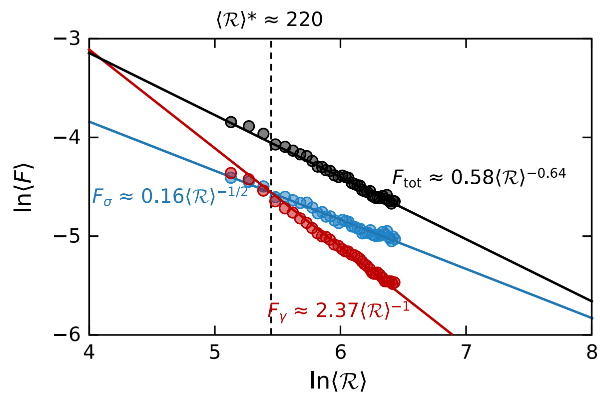

Fig. 10. Evolution of the average capillarity driving force (red circles), elastic driving force (blue circles) and total driving force (black circles) vs. mean grain size $\langle\mathcal{R}\rangle$ during GG. The red solid line is the fit to the classical capillarity law, $F \sim 1/\mathcal{R}$ (the fitted exponent is −0.90) and the blue solid line is $F \sim 1/\sqrt{\mathcal{R}}$ (the fitted exponent is −0.51). The black solid line is best fitted as $F \sim 1/\mathcal{R}^{-0.64}$. (For interpretation of the references to color in this figure legend, the reader is referred to the web version of this article.)

caused by the internal stress/disconnection flow — see an estimate in the SM).

Although our previously reported phase-field model [35–37] is employed here specifically to evaluate the effects of shear-coupling on grain growth, it does make some important assumptions that should be addressed in future to offer more physically complete descriptions. First, in our simulations we explicitly assume a fixed shear-coupling factor β on each GB. However, multiple disconnections modes, characterized by different magnitudes and signs of disconnection step heights and/or Burgers vectors, may be active [13,14,27]. The activation of multiple disconnection modes induces a dependence of the GB shear-coupling factor on the local stress state and GB curvature [21,66,67]. This mechanism will tend to reduce the elastic driving force, corresponding to a downward shift of the blue curve in Fig. 10, which is otherwise overestimated [27,68]. As a consequence, the resulting exponent n_F is expected to be closer to −1 than in the cases simulated here, while remaining larger, similar to the effect associated with the TJs discussed above. Note that this effect shifts the critical mean grain size, at which the capillarity-driven and elastic driving forces intersect, towards larger grain sizes.

The current model also neglects other possible stress relaxation pathways such as annealing twin formation [69,70] and dislocation emission from GBs [71,72] or TJs, which have been previously observed in molecular dynamics simulations [28]. Such emitted defects may interact with existing disconnections through disconnection annihilation, generation and/or reactions. This process may, in turn, relax part of the accumulated stress, such that the driving-force exponent n_F will be closer to the capillarity-driven limit (i.e., −1). Furthermore, GB migration will also affect plasticity within the grains; disconnections and their dynamics may modifies the ability of GBs to absorb, reflect or transmit dislocations, as we recently discussed [73,74]. GB motion and plasticity within grains should be treated as different aspects of an integrated whole, i.e., GBs should be treated as additional slip systems in a dislocation dynamics or crystal plasticity description. However, we exclude plasticity effects here to focus on the main question of the paper (i.e., "how does shear-coupling affect grain growth") and do not wish to complicate the case with other effects.

The coupling of stress and grain boundary motion is well established in quasi-two-dimensional polycrystals with nanoscale grains [14,27]. Fig. 10 shows that effects of shear-coupling become increasingly dominant with increasing grain size (in our two-dimensional simulations), consistent with observations that GB migration in three-dimensional micron-scale polycrystals deviates from curvature flow [15,75,76]. We note, however, that three-dimensional X-ray data reveal no internal strain above the noise floor ($\sim 0.1°$ lattice rotation) in microcrystalline samples [77], whereas thin-film experiments show larger rotations that should be detectable [14]. If strains are highly localized near GBs, they may evade X-ray detection, though such distributions are uncommon in higher-resolution GB studies. Dimensionality may influence results, as simulations in bicrystals show boundary-condition effects [28], and quasi two-dimensional films exhibit vertical displacements not mechanically accommodated in bulk materials [27]. Additional experiments and simulations are required to reveal the effect of dimensionality on shear-coupled motion in three-dimensional polycrystals.

5. Conclusions

We conducted a series of large-scale phase-field simulations to investigate and quantify the effects of internal and external stresses on GG, using a continuum model that reconciles curvature-driven and shear-coupled (disconnection-controlled) GB migration. We investigated (i) the evolution of the geometric and topological properties of the microstructures, (ii) the evolution of the internal stress field, and (iii) analyzed how these are correlated and can be reconciled with each other.

Our main conclusions are as follows.

1. Compared to microstructure evolution by mean-curvature flow alone, internal stress leads to less homogeneous and less equiaxed grains, enhanced GB faceting, increased grain aspect ratio, reduced grain roundness, and a shift of the grain-size distribution to smaller size, in agreement with experimental and atomistic results.
2. The average internal stress gradually relaxes during GG, with stress accumulation occurring around some TJs.
3. Grains with smaller internal stress tend to grow faster, whereas those with larger internal stress shrink faster.
4. Internal stress generation associated with GB shear-coupling tends to accelerate GG (i.e., produce larger GG exponents).
5. The application of external stress increases the grain aspect ratio, weakens GB faceting and grain roundness, and reduces the overall degree of internal-stress relaxation over time.

Overall, our results demonstrate that incorporating internal stress captures fundamental features of GG, as observed in experiments and atomistic simulations, which curvature flow alone fails to reproduce. The formulation underlying our model, grounded in disconnection-mediated GB migration, enables simulations of detailed microstructural features that result from both intrinsic driving forces in GG — curvature flow AND stress generation. The parameterization of our model, although minimal, is theoretically applicable to all FCC metals [37], and can be readily extended to other crystalline metals and even to ceramics by adjusting material-specific parameters.

CRediT authorship contribution statement

Caihao Qiu: Writing – review & editing, Writing – original draft, Visualization, Methodology, Investigation, Formal analysis, Data curation, Conceptualization. **David J. Srolovitz:** Writing – review & editing, Supervision, Resources, Funding acquisition, Formal analysis, Conceptualization. **Gregory S. Rohrer:** Writing – review & editing, Funding acquisition, Formal analysis, Conceptualization. **Jian Han:** Writing – review & editing, Supervision, Methodology, Funding acquisition, Formal analysis, Conceptualization. **Marco Salvalaglio:** Writing – review & editing, Writing – original draft, Supervision, Methodology, Funding acquisition, Formal analysis, Conceptualization.

Declaration of competing interest

The author Gregory S. Rohrer is Coordinating Editor for Acta Materialia and was not involved in the editorial review or the decision to publish this article. To avoid a conflict of interest, Gregory S. Rohrer was blinded to the record and another editor processed this manuscript.

Acknowledgments

CQ and DJS acknowledge support from the Hong Kong Research Grants Council Collaborative Research Fund C7140-25GF and General Research Fund 17210723 and 17200424. JH acknowledges General Research Fund from the Hong Kong Research Grants Council CityU 11213425. GSR acknowledges support by the National Science Foundation under DMREF Grant No. 2118945. MS acknowledges the support of the Deutsche Forschungsgemeinschaft (DFG, German Research Foundation) project No. 447241406 and 570666382.

Appendix A. Supplementary data

Supplementary material related to this article can be found online at https://doi.org/10.1016/j.actamat.2026.122494.

References

[1] J.K. Mason, E.A. Lazar, R.D. MacPherson, D.J. Srolovitz, Geometric and topological properties of the canonical grain-growth microstructure, Phys. Rev. E 92 (2015) 063308.
[2] J. Burke, D. Turnbull, Recrystallization and grain growth, Prog. Met. Phys. 3 (1952) 220.
[3] J. Von Neumann, Metal interfaces, Am. Soc. Met. Clevel. 108 (1952).
[4] W.W. Mullins, Two-dimensional motion of idealized grain boundaries, J. Appl. Phys. 27 (1956) 900.
[5] R.D. MacPherson, D.J. Srolovitz, The von Neumann relation generalized to coarsening of three-dimensional microstructures, Nature 446 (2007) 1053.
[6] J. Kim, N.C. Admal, Statistics of grain microstructure evolution under anisotropic grain boundary energies and mobilities using threshold-dynamics, Modelling Simul. Mater. Sci. Eng. 32 (2024) 035022.
[7] S.K. Naghibzadeh, Z. Xu, D. Kinderlehrer, R. Suter, K. Dayal, G.S. Rohrer, Impact of grain boundary energy anisotropy on grain growth, Phys. Rev. Mater. 8 (2024) 093403.
[8] M. Legros, D.S. Gianola, K.J. Hemker, In situ TEM observations of fast grain-boundary motion in stressed nanocrystalline aluminum films, Acta Mater. 56 (2008) 3380.
[9] J. Sharon, P. Su, F. Prinz, K. Hemker, Stress-driven grain growth in nanocrystalline Pt thin films, Scr. Mater. 64 (2011) 25.
[10] M. Winning, Grain boundary engineering by application of mechanical stresses, Scr. Mater. 54 (2006) 987.
[11] K. Harris, V. Singh, A. King, Grain rotation in thin films of gold, Acta Mater. 46 (1998) 2623.
[12] D. Farkas, S. Mohanty, J. Monk, Linear grain growth kinetics and rotation in nanocrystalline Ni, Phys. Rev. Lett. 98 (2007) 165502.
[13] C. Qiu, M. Salvalaglio, D.J. Srolovitz, J. Han, Disconnection flow–mediated grain rotation, Proc. Natl. Acad. Sci. 121 (2024a) e2310302121.
[14] Y. Tian, X. Gong, M. Xu, C. Qiu, Y. Han, Y. Bi, L.V. Estrada, E. Boltynjuk, H. Hahn, J. Han, et al., Grain rotation mechanisms in nanocrystalline materials: Multiscale observations in pt thin films, Science 386 (2024) 49.
[15] J. Zhang, W. Ludwig, Y. Zhang, H.H.B. Sørensen, D.J. Rowenhorst, A. Yamanaka, P.W. Voorhees, H.F. Poulsen, Grain boundary mobilities in polycrystals, Acta Mater. 191 (2020) 211.
[16] C. Qiu, M. Punke, Y. Tian, Y. Han, S. Wang, Y. Su, M. Salvalaglio, X. Pan, D.J. Srolovitz, J. Han, Grain boundaries are brownian ratchets, Science 385 (2024b) 980.
[17] J.W. Cahn, Y. Mishin, A. Suzuki, Coupling grain boundary motion to shear deformation, Acta Mater. 54 (2006) 4953.
[18] W. Bollmann, General geometrical theory of crystalline interfaces, Crystal Defects and Crystalline Interfaces, Springer, 1970, pp. 143–185.
[19] M. Ashby, Boundary defects, and atomistic aspects of boundary sliding and diffusional creep, Surf. Sci. 31 (1972) 498.
[20] J.P. Hirth, R.W. Balluffi, On grain boundary dislocations and ledges, Acta Metall. 21 (1973) 929.
[21] J. Han, S.L. Thomas, D.J. Srolovitz, Grain-boundary kinetics: A unified approach, Prog. Mater. Sci. 98 (2018) 386.
[22] A. Rajabzadeh, M. Legros, N. Combe, F. Mompiou, D. Molodov, Evidence of grain boundary dislocation step motion associated to shear-coupled grain boundary migration, Phil. Mag. 93 (2013) 1299.

[23] Q. Zhu, G. Cao, J. Wang, C. Deng, J. Li, Z. Zhang, S.X. Mao, In situ atomistic observation of disconnection-mediated grain boundary migration, Nat. Commun. 10 (2019) 1.
[24] R.C. Pond, S. Celotto, J.P. Hirth, A comparison of the phenomenological theory of martensitic transformations with a model based on interfacial defects, Acta Mater. 51 (2003) 5385.
[25] Y. Zheng, R.E.A. Williams, G.B. Viswanathan, W.A.T. Clark, H.L. Fraser, Determination of the structure of α-β interfaces in metastable β-Ti alloys, Acta Mater. 150 (2018) 25.
[26] Y. Qi, G. Richter, E. Suadiye, L. Klinger, E. Rabkin, Interdiffusion in bimetallic Au-Fe nanowhiskers controlled by interface mobility, Acta Mater. 197 (2020) 137.
[27] R. Gautier, F. Mompiou, O. Renk, C. Coupeau, N. Combe, G. Seine, M. Legros, Quantifying grain boundary deformation mechanisms in small-grained metals, Nature 648 (2025) 327.
[28] S.L. Thomas, K. Chen, J. Han, P.K. Purohit, D.J. Srolovitz, Reconciling grain growth and shear-coupled grain boundary migration, Nat. Commun. 8 (2017) 1.
[29] Y.-B. Guo, T. Xu, M. Li, Generalized type iii internal stress from interfaces, triple junctions and other microstructural components in nanocrystalline materials, Acta Mater. 61 (2013) 4974.
[30] N.C. Admal, G. Po, J. Marian, A unified framework for polycrystal plasticity with grain boundary evolution, Int. J. Plast. 106 (2018) 1.
[31] J. He, N.C. Admal, Polycrystal plasticity with grain boundary evolution: A numerically efficient dislocation-based diffuse-interface model, Modelling Simul. Mater. Sci. Eng. 30 (2021) 025006.
[32] G. Huang, A. Mensah, M. Chlupsa, Z. Croft, L. Qi, A.J. Shahani, K. Thornton, Phase-field modeling of stored-energy-driven grain growth with intra-granular variation in dislocation density, Modelling Simul. Mater. Sci. Eng. 32 (2024) 045011.
[33] M. Gokuli, B. Runnels, Multiphase field modeling of grain boundary migration mediated by emergent disconnections, Acta Mater. 217 (2021) 117149.
[34] D. Bugas, B. Runnels, Grain boundary network plasticity: Reduced-order modeling of deformation-driven shear-coupled microstructure evolution, J. Mech. Phys. Solids 184 (2024) 105541.
[35] J. Han, D.J. Srolovitz, M. Salvalaglio, Disconnection-mediated migration of interfaces in microstructures: I. continuum model, Acta Mater. 227 (2022) 117178.
[36] M. Salvalaglio, D.J. Srolovitz, J. Han, Disconnection-mediated migration of interfaces in microstructures: Ii. diffuse interface simulations, Acta Mater. 227 (2022) 117463.
[37] C. Qiu, D.J. Srolovitz, G.S. Rohrer, J. Han, M. Salvalaglio, Why grain growth is not curvature flow, Proc. Natl. Acad. Sci. 122 (2025) e2500707122.
[38] R.T. Dehoff, Topography and microstructure, Metallography 8 (1975) 71.
[39] S.K. Kurtz, F. Carpay, Microstructure and normal grain growth in metals and ceramics. part ii. experiment, J. Appl. Phys. 51 (1980) 5745.
[40] V. Fradkov, A. Kravchenko, L. Shvindlerman, Experimental investigation of normal grain growth in terms of area and topological class, Scr. Metall. 19 (1985) 1291.
[41] K. Barmak, E. Eggeling, D. Kinderlehrer, R. Sharp, S. Ta'asan, A. Rollett, K. Coffey, Grain growth and the puzzle of its stagnation in thin films: The curious tale of a tail and an ear, Prog. Mater. Sci. 58 (2013) 987.
[42] D. Srolovitz, M.P. Anderson, P.S. Sahni, G.S. Grest, Computer simulation of grain growth—ii. grain size distribution, topology, and local dynamics, Acta Metall. 32 (1984) 793.
[43] G.S. Grest, M.P. Anderson, D.J. Srolovitz, Domain-growth kinetics for the q-state potts model in two and three dimensions, Phys. Rev. B 38 (1988) 4752.
[44] P. Mulheran, J. Harding, A simple statistical model for grain growth in materials, Acta Met. et Mater. 39 (1991) 2251.
[45] D. Fan, C. Geng, L.-Q. Chen, Computer simulation of topological evolution in 2-d grain growth using a continuum diffuse-interface field model, Acta Mater. 45 (1997) 1115.
[46] C.E. Krill I.I.I., L.-Q. Chen, Computer simulation of 3-d grain growth using a phase-field model, Acta Mater. 50 (2002) 3059.
[47] R.D. Kamachali, I. Steinbach, 3-d phase-field simulation of grain growth: Topological analysis versus mean-field approximations, Acta Mater. 60 (2012) 2719.
[48] E.A. Lazar, R.D. MacPherson, D.J. Srolovitz, A more accurate two-dimensional grain growth algorithm, Acta Mater. 58 (2010) 364.
[49] E.A. Lazar, J.K. Mason, R.D. MacPherson, D.J. Srolovitz, A more accurate three-dimensional grain growth algorithm, Acta Mater. 59 (2011) 6837.
[50] E.A. Lazar, J.K. Mason, R.D. MacPherson, D.J. Srolovitz, Distribution of topological types in grain-growth microstructures, Phys. Rev. Lett. 125 (2020) 015501.
[51] R. Backofen, K. Barmak, K. Elder, A. Voigt, Capturing the complex physics behind universal grain size distributions in thin metallic films, Acta Mater. 64 (2014) 72.
[52] G.M. La Boissonière, R. Choksi, K. Barmak, S. Esedḡolu, Statistics of grain growth: experiment versus the phase-field-crystal and mullins models, Materialia 6 (2019) 100280.
[53] X. Zhong, M.N. Kelly, H.M. Miller, S.J. Dillon, G.S. Rohrer, Grain boundary curvatures in polycrystalline srtio3: Dependence on grain size, topology, and crystallography, J. Am. Ceram. Soc. 102 (2019) 7003.
[54] I. Steinbach, F. Pezzolla, A generalized field method for multiphase transformations using interface fields, Phys. D: Nonlinear Phenom. 134 (1999) 385.
[55] I. Steinbach, Phase-field models in materials science, Modelling Simul. Mater. Sci. Eng. 17 (2009) 073001.
[56] G. Gottstein, L. Shvindlerman, The compensation effect in thermally activated interface processes, Interface Sci. 6 (1998) 267.
[57] C. Qiu, M. Salvalaglio, D.J. Srolovitz, J. Han, Interface faceting-defaceting mediated by disconnections, Acta Mater. 251 (2023) 118880.
[58] T. Radetic, C. Ophus, D. Olmsted, M. Asta, U. Dahmen, Mechanism and dynamics of shrinking island grains in mazed bicrystal thin films of Au, Acta Mater. 60 (2012) 7051.
[59] S. Dillon, H. Miller, M.P. Harmer, G.S. Rohrer, Grain boundary plane distributions in aluminas evolving by normal and abnormal grain growth and displaying different complexions, Int. J. Mat. Res 101 (2010) 1.
[60] L. Zhang, J. Han, Y. Xiang, D.J. Srolovitz, Equation of motion for a grain boundary, Phys. Rev. Lett. 119 (2017) 246101.
[61] P. Anderson, J. Hirth, J. Lothe, Theory of Dislocations, Cambridge University Press, 2017, http://www.worldcat.org/oclc/1132912878.
[62] S.L. Thomas, C. Wei, J. Han, Y. Xiang, D.J. Srolovitz, Disconnection description of triple-junction motion, Proc. Natl. Acad. Sci. 116 (2019) 8756.
[63] E. Hall, The deformation and ageing of mild steel: Iii discussion of results, Proc. Phys. Soc. Sect. B 64 (1951) 747.
[64] J. Yin, D.M. Barnett, S.P. Fitzgerald, W. Cai, Computing dislocation stress fields in anisotropic elastic media using fast multipole expansions, Modelling Simul. Mater. Sci. Eng. 20 (2012) 045015.
[65] H. Zhang, M. Mendelev, D. Srolovitz, Computer simulation of the elastically driven migration of a flat grain boundary, Acta Mater. 52 (2004) 2569.
[66] K. Chen, J. Han, S.L. Thomas, D.J. Srolovitz, Grain boundary shear coupling is not a grain boundary property, Acta Mater. 167 (2019) 241.
[67] C. Wei, S.L. Thomas, J. Han, D.J. Srolovitz, Y. Xiang, A continuum multi-disconnection-mode model for grain boundary migration, J. Mech. Phys. Solids 133 (2019) 103731.
[68] R. Gautier, A. Rajabzadeh, M. Larranaga, N. Combe, F. Mompiou, M. Legros, Shear-coupled migration of grain boundaries: the key missing link in the mechanical behavior of small-grained metals?, Comptes Rendus. Phys. 22 (2021) 19.
[69] R. Fullman, J. Fisher, Formation of annealing twins during grain growth, J. Appl. Phys. 22 (1951) 1350.
[70] S.L. Thomas, A.H. King, D.J. Srolovitz, When twins collide: Twin junctions in nanocrystalline nickel, Acta Mater. 113 (2016) 301.
[71] J.C. Li, Mechanical grain growth in nanocrystalline copper, Phys. Rev. Lett. 96 (2006) 215506.
[72] G.B. Bizana, L.A. Barrales-Mora, Kinetics of grain boundary migration in nanosized Al polycrystals, Acta Mater. 260 (2023) 119261.
[73] J. Yu, A.H. Ngan, D.J. Srolovitz, J. Han, Application of rigorous interface boundary conditions in mesoscale plasticity simulations, Modelling Simul. Mater. Sci. Eng. 32 (2024) 035020.
[74] J. Yu, A.H. Ngan, D.J. Srolovitz, J. Han, Mesoscale description of interface-mediated plasticity, Acta Mater. 283 (2025) 120552.
[75] Z. Xu, Y.-F. Shen, S.K. Naghibzadeh, X. Peng, V. Muralikrishnan, S. Maddali, D. Menasche, A.R. Krause, K. Dayal, R.M. Suter, et al., Grain boundary migration in polycrystalline α-Fe, Acta Mater. 264 (2024) 119541.
[76] Z. Xu, F. Abdeljawad, G.S. Rohrer, Can the grain boundary stiffness driving force explain observed grain boundary migration rates in polycrystals?, Scr. Mater. 274 (2026) 117135.
[77] A. Bhattacharya, Y.-F. Shen, C.M. Hefferan, S.F. Li, J. Lind, R.M. Suter, C.E. Krill I.I.I., G.S. Rohrer, Grain boundary velocity and curvature are not correlated in Ni polycrystals, Science 374 (2021) 189.